Air-Bridged Gate MESFET: A New Structure to Reduce Wave Propagation Effects in High-Frequency Transistors

Samir M. Hammadi, *Student Member, IEEE,* and Samir M. El-Ghazaly, *Senior Member, IEEE*

***Abstract*—In conventional microwave transistors, the gain and output power are significantly reduced by gate ohmic resistance and phase cancellation. The air-bridged gate (ABG) transistors overcomes both problems by providing larger gate cross section along the propagation direction of the signal, and keeping both the input and output signals in phase along the device width. The performance of the air-bridged and conventional transistor is evaluated from both dc and radio-frequency (RF) points-of-view. A full hydrodynamic transport model, which accurately describes the electron dynamics in short channel devices, is used in the dc analysis. For RF analysis, a full-wave model, capable of capturing all important high-frequency effects, such as wave-particle interactions and traveling-wave effects, is implemented. This model is based on the coupling of the hydrodynamic transport equations with Maxwell's equations. Results related to the traveling-wave effects in conventional and ABG devices, such as phase mismatch and gain reduction at high frequencies, are illustrated. From these results, we show that the ABG metal–semiconductor field-effect transistor (MESFET) has superior performance at very high frequency as compared to conventional planar MESFET's.**

***Index Terms*— Air-bridged gate MESFET, full-wave simulation, global modeling.**

I. Introduction

THE impressive progress in microwave technology witnessed over the past few years led to the development of several types of microwave transistors with miniaturized features. The push toward smaller size devices is triggered by the drive to operate at higher frequencies and achieve better gains. The performance of microwave transistors is largely controlled by three parameters; namely: 1) the gate length; 2) the device width; and 3) the active layer characteristics. By using smaller gate lengths, both the electron transit time and gate-to-source capacitance are reduced, thereby, providing higher cutoff frequencies of the device. On the other hand, increasing the device width leads to better gains because of the added distributed conductance effect. The device gain, however, does not increase indefinitely with the device width. In fact, there is a tradeoff cost associated with the down sizing of the gate length and stretched width of the device. First, the reduced cross section of the gate electrode and its increased width results in a significant increase in the gate metallic resistance, which creates a real concern about access signal attenuation along the width of the device. In additions, further degradation of the device performance may arise at high frequencies due to phase mismatch between the gate and drain signals and from wave reflection at the electrodes open ends. The phase mismatch is a result of the different input impedances at the gate and drain electrodes.

Full understanding of the traveling-wave effects in small-size high-frequency transistors require special attention because of complex electron dynamics and the passive and active coupling inside the device. Accurate models of these devices require the inclusion of electromagnetic (EM) wave effects, which can be fulfilled using a full-wave approach. Generally, full-wave models used for the analysis of distributed effects in microwave transistors are based on coupled-mode theory [1]–[4]. In this modeling approach, small-signal equivalent-circuit parameters are either measured or computed using quasi-static semiconductor physical models. The equivalent circuit is then used to generate a distributed circuit model for the device, which is then analyzed using transmission-line theory. This approach, however, provides accurate results only within the range where the extracted equivalent-circuit parameters remain valid. In addition, the accuracy of this approach may be questionable at very high frequencies because of the various approximations used in the physical semiconductor model. In such models, it is generally assumed that device dimensions are much smaller than the operating wavelength, which becomes an invalid assumption at high operating frequencies. Moreover, at very high frequencies, energy and momentum relaxation times of charge carriers become comparable to the EM wavelength and because electrons need a finite time to respond to field variations, the electron transport is directly affected by the propagating wave. This, in turn, affects the device operation, particularly under transient and large-signal conditions. These aforementioned facts clearly indicate that wave–particle interactions and their effect on the device operation can no longer be ignored and that new models capable of simulating these interactions should be considered. An effort has already been extended toward that end by Al-Sunaidi *et al.* [5], [6]. In [6], Al-Sunaidi presented a full-wave physical model for high-frequency transistors that integrates the semiconductor transport equations with direct solution of Maxwell's equations. The model philosophy is basically to use charge carriers, solved for using semiconductor transport equations, as sources in Maxwell's equations. The

Manuscript received February 12, 1999. This work was supported by the Army Research Office under Contract DAAD 19-99-1-0194.

The authors are with the Department of Electrical Engineering, Arizona State University, Tempe, AZ 85281-5706 USA.

Publisher Item Identifier S 0018-9480(99)04455-5.

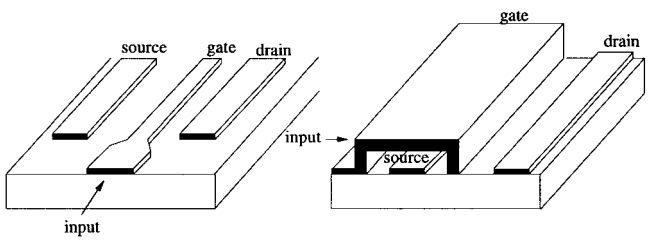

Fig. 1. (a) Conventional MESFET. (b) ABG MESFET.

fields obtained from the solution to Maxwell's equations are then fed back into the transport equations as driving forces. The same model was later used by Imtiaz and El-Ghazaly in [7] for the analysis of microwave amplifiers. It is our believe that this new look into device modeling, which calls for a global modeling approach, is the way that will lead to the next generation of high-frequency transistor models.

The usual approach to overcome the effect of the gate metallic resistance is to use several gate fingers in parallel. The disadvantage of this approach is the resulting low input and output impedances, which can create a matching problem for the device. Also, synchronizing the phase on the different fingers and the increased interference may cause additional problems as the frequency increases. To increase its cross section, the gate is usually made long in a mushroom-like shape with a very thin base. Eventually, this results in a very fragile gate electrode that may brake easily. In [8], El-Ghazaly *et al*. suggested a new device geometry, the inverted-gate field-effect transistor (INGFET), in an attempt to reduce both the gate resistance and phase mismatch problems. By making the device symmetric with respected to the gate electrode and operating the device in a common gate mode, the input impedances of the source and drain are made equal and, consequently, the signals at both electrodes will propagate with exactly the same phase velocities. Moreover, the inverted gate cross section can be made very large in order to reduce its resistance. This device, however, remains questionable from a practical point-of-view due to the additional process variations it requires for fabrication.

Another approach to eliminate the distributed effects and solve the gate resistance problem at the same time, is instead driving the device at one end, as shown in Fig. 1(a), the device is driven along its width using an air-bridged gate (ABG) [9], as shown in Fig. 1(b). In this case, the wave travels transversely along the device length with a constant phase velocity; thereby, avoiding any effects due to phase mismatch. Moreover, because the device length is much smaller than the wavelength, distributed effects are negligible even at very high frequencies. The ABG metal–semiconductor field-effect transistor (MESFET) also solves the problems associated with the gate metallic resistance. Since the signal is fed along the device width, the gate cross section perpendicular to the signal direction of propagation can be made large enough to reduce the gate resistance to a minimum by increasing the gatewidth.

This paper presents a detailed analysis of the ABG MESFET. A two-dimensional (2-D) full-hydrodynamic model is used to investigate the dc characteristics of a GaAs air-bridged MESFET. The model is solved without the usual simplifying assumptions on the electron energy or momentum equations; thereby, including all hot-electron and inertia effects in the electron transport. The dc characteristics of the air-bridged MESFET are compared with those of the conventional MESFET.

It is also the objective of this paper to build on the work pioneered by our group and present a more mature version of full-wave physical models based on the same previously mentioned modeling philosophy. More results highlighting the traveling-wave effects, e.g., propagation constant, attenuation constant, and phase velocity mismatch, are generated using this model. The model is simulated using the FDTD method, encouraged in doing so by the simplicity and versatility of the method and the availability of powerful computers that allow the simulation to be carried in reasonable times.

Finally, we should bring to the attention of the reader that the ABG structure is intended for very high-frequency applications using high electron-mobility transistors (HEMT's). The fact that we based our analysis on a MESFET is for convenience and illustrative purposes only. The radio-frequency (RF) properties of all field-effect transistors are very similar, and our results for the MESFET device are also valid for several other high mobility devices such as HEMT's.

II. Device Model

The combination of small size and high operating frequency (characteristic of modern-day microwave transistors) make the traditional circuit and physical models, where electron transport is viewed in total separation from EM-wave effects, unacceptable. For such devices, integrated full-wave physical modeling approach is required for accurate device design, optimization, and characterization. In this section, we first present a brief review of the semiconductor transport model. The model developed is a full hydrodynamic model with no simplifying assumptions on the energy or momentum equations. As a results, the model accurately describes electron transport in short-channel devices. Full details of this model can be found in [30]. Next, the main features of the full-wave model are presented. This model is based on the coupling between Maxwell's equations and the semiconductor transport equation. Additional information on this modeling approach and applications can be found in [6] and [7].

A. DC Semiconductor Model

The semiconductor transport model is based on the semi-classical hydrodynamic model that states conservation of particles, momentum, and energy. The conservation equations are obtained by proper integration of the Boltzmann's transport equation over the momentum space and averaging over the multivalley conduction band. Time relaxation approximation is used for the collision terms, and minority charge transport, as well as generation/recombination effects, are neglected. The resulting equations constitute a set of nonlinear and strongly coupled partial differential equations. Together with Poisson's equation, they form a complete time-dependent self-consistent set of equations that can be solved for the dc solution of

electron density, momentum, and energy. The complete set of equations are as follows.

- *Continuity Equation*

$$\frac{\partial n}{\partial t} + \nabla \cdot (n\vec{v}) = 0. \tag{1}$$

- *Energy Conservation Equation*

$$\frac{\partial (n\varepsilon)}{\partial t} + \nabla \cdot (n\vec{v}\varepsilon) = -qn\vec{v} \cdot \vec{E} - \nabla \cdot (nkT\vec{v}) - \frac{n(\varepsilon - \varepsilon_0)}{\tau_\varepsilon(\varepsilon)}. \tag{2}$$

- *Momentum Conservation Equation*

$$\frac{\partial (np_x)}{\partial t} + \nabla \cdot (np_x\vec{v}) = -qnE_x - \frac{\partial (nkT)}{\partial x} - \frac{np_x}{\tau_m(\varepsilon)}. \tag{3}$$

- *Poisson's Equation*

$$\nabla^2 V = -\rho/\epsilon \tag{4}$$

where τ_m and τ_e are the momentum and energy relaxation times, respectively. These are energy dependent and their values are obtained from steady-state Monte Carlo simulation. T is the electron temperature, q is the electronic charge, and k is the Boltzmann's constant. Similar expressions are obtained for the other momentum components (i.e., y- and z-components). The current density distribution inside the device is given by

$$\vec{J} = -qn\vec{v}. \tag{5}$$

This model accurately describes all nonstationary transport effects by allowing energy dependence of all transport parameters such as effective mass and relaxation times. The inertia effects, which are usually neglected in most existing models, are also included by allowing the electron momentum to be time and space dependent. Another commonly used assumption that is eliminated here is the constant effective mass approximation. The effective mass variation with respect to time, space, and energy are all included in this model.

B. Full-Wave Model

The full-wave model is used to describe the wave–particle interaction inside the semiconductor device as well as the traveling-wave effects along the device width. The EM-wave distribution is obtained by direct solution of Maxwell's equations. The charge carriers distribution is obtained from the solution of the hydrodynamic model described earlier. Coupling between the two models is done by using the charge carries as sources of the EM field inside Maxwell's equations. On the other hand, the fields are used as forcing functions in the semiconductor model.

Fig. 2 shows the different steps involved in the full-wave model simulation. The first step is the initialization process. In this step, all transport parameters, electronic densities, and dc fields, due to fixed bias, are computed. All quantities are evaluated from the steady-state simulation of the semiconductor model. The initialization process is essential for two reasons. First, it allows the full-wave simulation of the device to be carried at a well defined bias point, by using

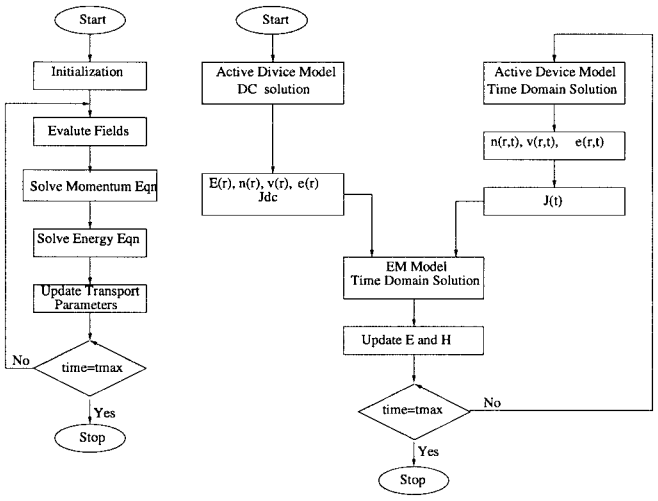

(a) (b)

Fig. 2. Steps involved in full-wave simulation. (a) Initialization step. (b) Iterative coupling step.

the proper initial values for the different electronic quantities, transport parameters, and dc fields. In quasi-static models, this is done by simply specifying bias voltages at the device electrodes. Second, since direct solution of Maxwell's equations inherently rejects all dc components, the initialization process provides the correct approach to compute the total field inside the device. This total field is equal to the time-varying field, computed from Maxwell's equations, plus the dc field provided by the steady-state simulation of the semiconductor model. The field inside the device is then given by the expression

$$\vec{E} = \vec{E}^{\rm dc} + \vec{E}^{M} \tag{6}$$

where $E^{\rm dc}$ is the dc field computed in the initialization step, and E^{M} is the time-varying field provided by Maxwell's equations.

The second step corresponds to the iterative coupling between the transport equations and Maxwell's equations. In this step, Maxwell's equations replace Poisson's equations, used in the steady-state model, for the updating of the electric and magnetic fields in the device. The two Maxwell's equations used in the full-wave model are the two curl equations given by

$$\frac{\partial \vec{E}}{\partial t} = \frac{1}{\epsilon}\Big(\nabla \times \vec{H} - (\vec{J}^{\rm tot} - \vec{J}^{\rm dc})\Big) \tag{7}$$

$$\frac{\partial \vec{H}}{\partial t} = -\frac{1}{\mu}\nabla \times \vec{E}. \tag{8}$$

In (7), $J^{\rm dc}$ is the dc current density computed from steady-state simulation of step (1). $J^{\rm tot}$ is the current density obtained from the full-wave simulation.

At this point, it is important to stress the fact that this model is valid for both small- and large-signal analyses. Decomposing the fields into steady-state and time-varying components does not limit the analysis to small signals only, and the device can still be driven into nonlinear region. As previously mentioned, the field decomposition is needed to avoid problems with the numerical solutions of Maxwell's equations by removing the nonpropagating dc components.

C. Numerical Solution

Both the steady-state semiconductor model and the full-wave model were solved numerically using an FDTD scheme. The FDTD method was chosen because it is simple and it allows great flexibility in the simulation of structures with complex geometries such as the ABG devices. In the following, we briefly review the solution method of each model and describe the structures of the various simulated devices.

1) Solution of Hydrodynamic Equations: The semiconductor conservation equations are solved in conjunction with Poisson's equation, in an iterative manner until a steady-state solution is reached. An explicit finite-difference time-domian (FDTD) scheme was used to discretize each equation. To maintain stability, the space increment is chosen to be on the order of the Debye length. The set of conservation equations are discretized using first- and second-order upwind schemes in order to preserve the transportive and conservative properties of the differential equations. More details of the discretization method of each term in the conservation equations can be found in [5]. The solution is carried on a 2-D mesh with nonuniform spacing along the y-direction and uniform spacing along the x-direction. This type of grid was used because of the need to include a large air region in the computation domain on top of the semiconductor device. At each iteration step, the Poisson's equation is solved iteratively using a successive-order-relaxation (SOR) method with a relaxation factor on the order of 1.8.

2) Solution of Maxwell's Equations: The time-domain solution of Maxwell's equations is obtained using a three-dimensional (3-D) mesh where field components are arranged according to Yee's algorithm [21]. The time step dt and the space cell size in each direction are chosen so that stability and low numerical dispersion are insured. To minimize dispersion, the space increments are taken less than 1/10 of the minimum wavelength contained in the excitation source signal [31]. The structure is terminated with absorbing boundary conditions along each side. Perfectly matched layer (PML) absorbing boundaries were used along the z-direction, which is the direction of propagation of the wave, while first-order Mur absorbing boundaries are used along the remaining sides.

3) Simulated Structure: Fig. 3 shows the 2-D structures used in the dc simulation of both the ABG and conventional MESFET transistors. A nonzero metal thickness is used to model the device electrodes in both cases. A T-shape gate electrode is used to approximate the mushroom-shape gate cross sections used in the actual devices. An air region is included in the simulation domain to account for any parasitic capacitance due to the fringing fields between the different electrodes.

Fig. 4 shows the 3-D structure used in the full-wave simulation. Since we are only interested in the traveling-wave effects, the metallic electrodes are assumed to be lossless and of zero thickness.

III. Results and Discussion

All devices considered in this simulation consist of an active layer of 0.1-μm thickness with doping density of

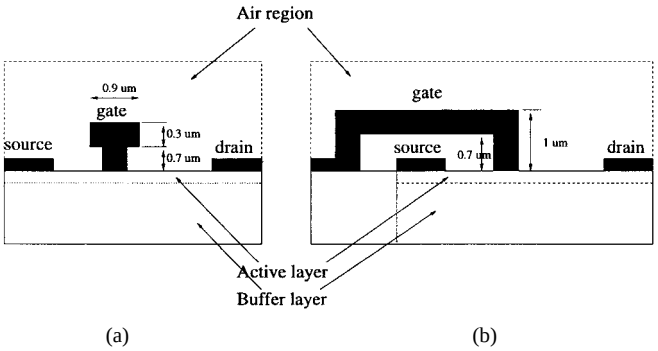

Fig. 3. 2-D structure used in dc-simulations. (a) Conventional MESFET. (b) ABG MESFET.

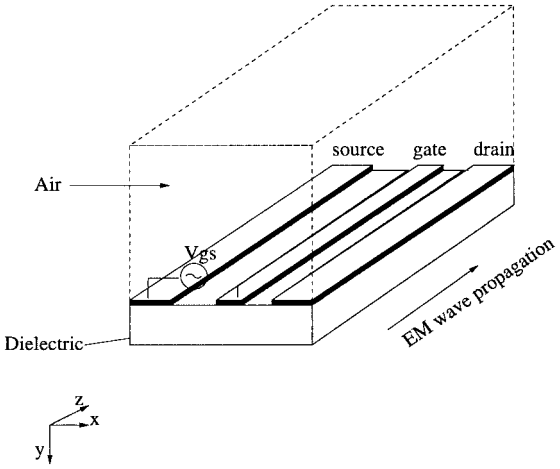

Fig. 4. 3-D structure of the MESFET.

TABLE I
MESFET Simulation Parameters.

Drain and source contacts	$0.5\mu m$
Gate-source separation	$0.5\mu m$
Gate-drain separation	$1\mu m$
Device thickness	$0.4\mu m$
Active layer thickness	$0.1\mu m$
Active layer doping	$2 \times 10^{17} cm^{-3}$
Substrate doping	$10^{14} cm^{-3}$
Schotky barrier height	$0.8V$

2×10^{17} cm^{-3}. The doping of the buffer layer is taken to be 10^{14} cm^{-3} and the doping profile between the active and buffer layers is assumed abrupt. A gate length of 0.3 μm was used, with 0.5-μm gate-to-source separation and 1-μm gate-to-drain separation. The built-in potential at the Schottky contact under the gate is set to 0.8 V. The source and drain electrodes are assumed to form perfect ohmic contacts with the semiconductor region. The lattice temperature is taken equal to 300 K. Table I summarizes all the important physical parameters used in the simulation.

A. DC Simulation Results

Evaluation of the air-bridged MESFET performance is first done from the dc point-of-view. Results for the dc drain current and small-signal parameters are generated from the steady-state simulation and compared with the corresponding

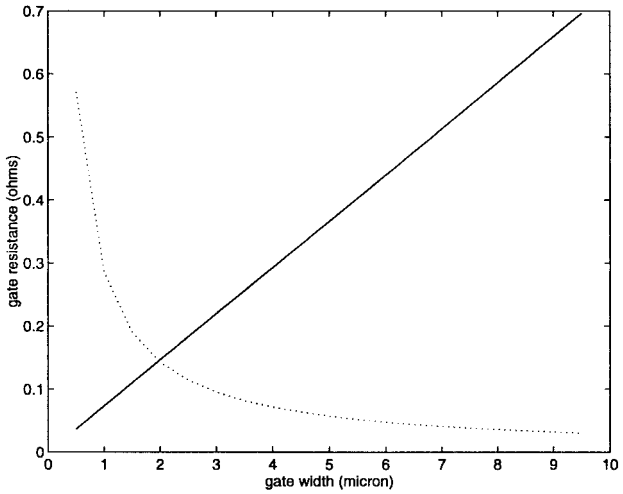

Fig. 5. The gate metallic resistance as a function of the gatewidth. Solid line: Conventional MESFET. Dotted line: ABG MESFET.

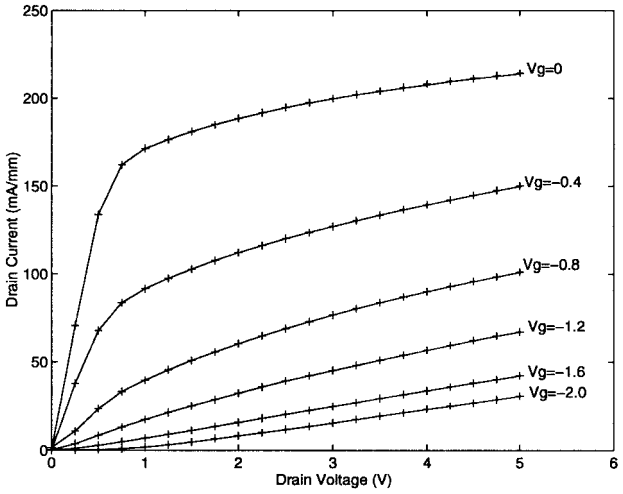

Fig. 6. *I–V* characteristics of both conventional MESFET (+++) and air-bridged MESFET (solid line).

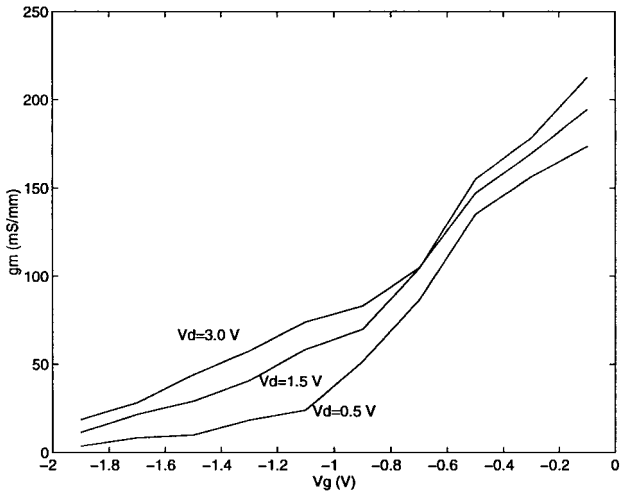

Fig. 7. Results for the transconductance g_m of the ABG MESFET.

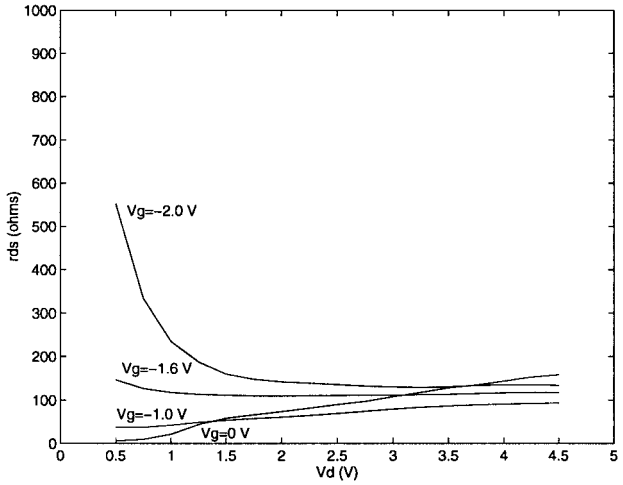

Fig. 8. Results for the output resistance $r\mathrm{ds}_m$ of the ABG MESFET.

results obtained for a conventional MESFET. As indicated in the introduction, a key feature of the ABG device is its low gate resistance, as compared to a conventional devices. This fact is illustrated in Fig. 5, which shows the variation of the gate resistance with the gate length for each device. As the figure shows, for the air-bridged MESFET, the gate resistance decreases as we increase the device width; whereas for the conventional MESFET, the gate resistance increases linearly with the device width. In Fig. 6, we show the results for the *I–V* characteristic of both devices. It is interesting to observe that both devices have almost exactly identical characteristics. This may be explained by the fact that the dc current is mainly controlled by the field strength and the electron distribution inside the device. On the other hand, using an ABG instead of the mushroom gate had little effect on the steady-state distribution of these quantities. From these results, we expect that the same observation is true for all small signal parameters that are extracted from values of the drain current and bias voltages, e.g., transconductance and intrinsic output resistance. The computed values of the two latter parameters are shown in Figs. 7 and 8. As in the case of a conventional device, we observe the strong dependence of the transconductance on bias voltages, whereas the values of the output resistance are less sensitive to bias conditions. Results for the gate-to-source capacitance C_{gs} as a function of bias voltages are illustrated in Fig. 9. The figure indicates that the air-bridged MESFET has higher C_{gs} values than the conventional one. This result is expected because of the higher parasitic capacitance in the case of the air-bridged MESFET. For this device, the effective area between the source and drain is increased, while the effective distance between the two electrodes is reduced, therefore, leading to higher capacitance values. Since the cutoff frequency f_t of the device is proportional to the transconductance, and inversely proportional to the gate-to-source capacitance, we deduce from the results obtained for C_{gs} and g_m that the air-bridged MESFET has lower cutoff frequency than the conventional MESFET. This result is depicted in Fig. 10, which shows the variation of f_t with V_{gs} for a drain voltage $V_d = 3$ V for both devices. From this figure, we also notice that the difference between the two cutoff frequencies is higher at higher V_{gs} values. We already indicated that both devices have identical

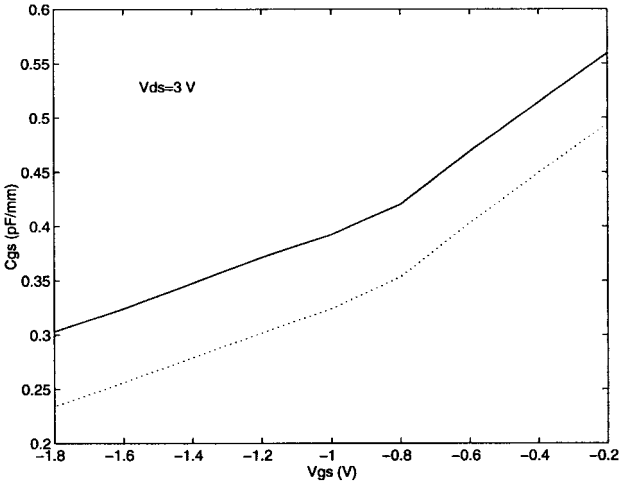

Fig. 9. $C_{\rm gs}$ as a function of $V_{\rm gs}$ for $V_{\rm ds} = 3.0$ V. $C_{\rm gs}$ for conventional MESFET (dashed line). $C_{\rm gs}$ for ABG MESFET (dotted line).

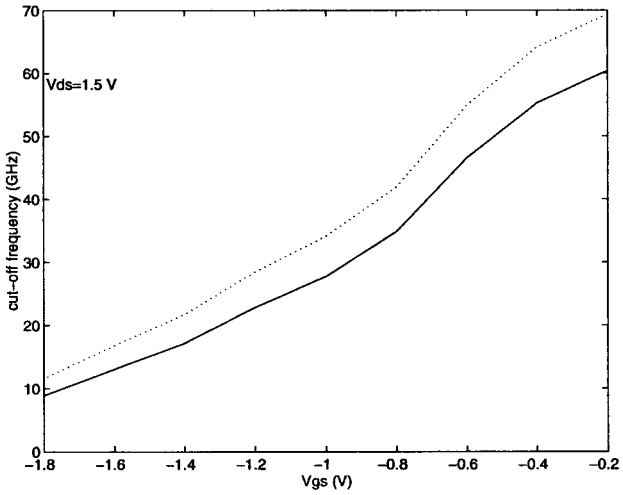

Fig. 10. Cutoff frequency F_t as a function of $V_{\rm gs}$ for $V_{\rm ds} = 1.5$ V F_t for conventional MESFET (dashed line). F_t for ABG MESFET (dotted line).

transconductance values and, therefore, the different rates of change for f_t portrayed by the two devices is attributed to the different rates of change of $C_{\rm gs}$ with the voltage $V_{\rm gs}$. In fact, the air-bridged MESFET has $C_{\rm gs}$ values that increases with $V_{\rm gs}$ at a higher rate than a conventional MESFET. In addition, one might add the fact it is the intrinsic part of $C_{\rm gs}$ that is responsible for such a type of change since the parasitic part depends only on the electrodes geometry and, therefore, is constant with $V_{\rm gs}$. Finally, from Fig. 11, we notice that the air-bridged MESFET has lower $C_{\rm gd}$ values than the conventional MESFET. Again, this may be explained by the fact that the effective area between gate and drain is smaller in the case of the air-bridged MESFET.

By simply considering the above dc analysis, one may come to the conclusion that conventional MESFET devices are far better than the air-bridged MESFET. Although this might be true for low-frequency applications, these results say little about the RF performance of each device at high frequencies. It would, therefore, be very simplistic to just project these conclusions for high-frequency applications. In fact, this is the

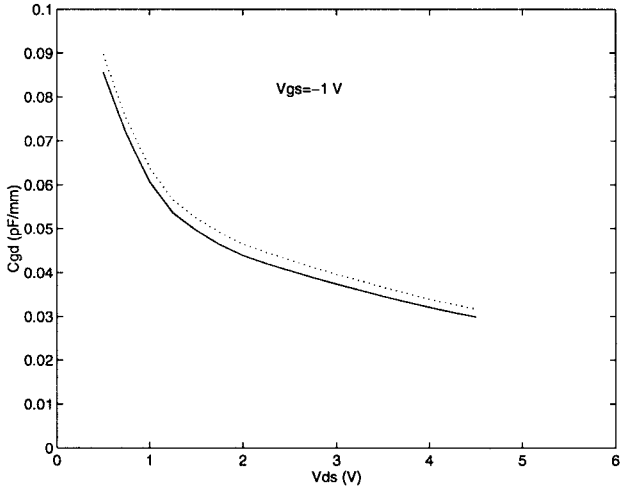

Fig. 11. $C_{\rm gd}$ as a function of $V_{\rm ds}$ for $V_{\rm gs} = -1.0$ V $C_{\rm gd}$ for conventional MESFET (dashed line). $C_{\rm gd}$ for ABG MESFET (dotted line).

exact message that this paper is intended to convey, namely that traditional physics-based models, where electron transport is viewed in total separation from the EM-wave effect, are not adequate to accurately simulate the state-of-art high-frequency devices. The purpose of Section III-B, which looks into the device performance from RF point-of-view, is to justify this statement.

B. Full-Wave Simulation of the Planar MESFET

For the full-wave analysis, a time-domain Gaussian pulse is applied between the source and gate. An added type of source is used at the excitation plane. The field distribution at the source plane is given by the following expression:

$$E_s^{n+1} = E_s^n + \alpha \Psi(x,y) e^{\frac{(t-t_0)^2}{T^2}} \tag{9}$$

where α is a factor between zero and one, and $\Psi(x,y)$ is the 2-D template representing the field distribution of the desired mode. This source model is found to give good results even if it is in the vicinity of some type of discontinuity. This is because the source plane is transparent to any back reflections and does not cause any spurious retroflections that may contaminate the field distribution and lead to erroneous results.

The input and output time-domain signals are observed at different points along the device width. The input voltage is taken between the source and gate, and the output voltage is the voltage between the source and drain. Frequency-dependent parameters such as gain and propagation constants are computed using Fourier transforms of the time-domain data in a manner similar to that described in [32]. Assuming a wave propagation of the form $e^{-\gamma z}$, the propagation constant can then be evaluated as follows:

$$\gamma = \frac{1}{z_1 - z_2} \log\left(\frac{F(\omega, z_1)}{F(\omega, z_2)}\right) \tag{10}$$

where $F(\omega, z_i)$ is the Fourier transform of the time-domain signal at $z = zi$. The phase and attenuation constants can then be evaluated as the imaginary and real parts of γ. For the computation of the device gain, we adopted the following

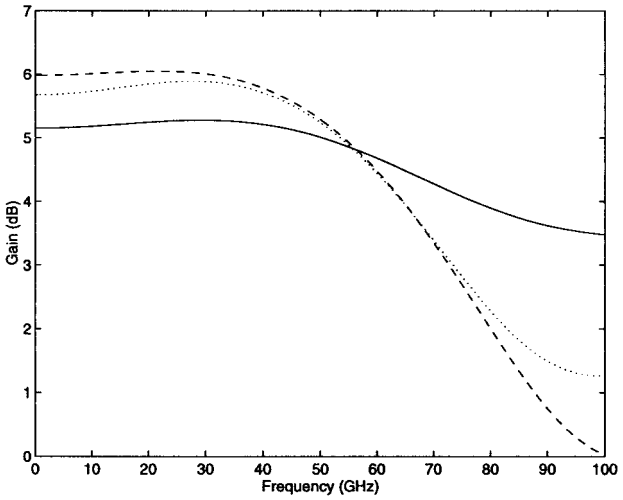

Fig. 12. RF gain of the MESFET as a function of frequency. Device width $= 100$ μm (solid line), 250 μm (dotted line), and 400 μm (dashed line).

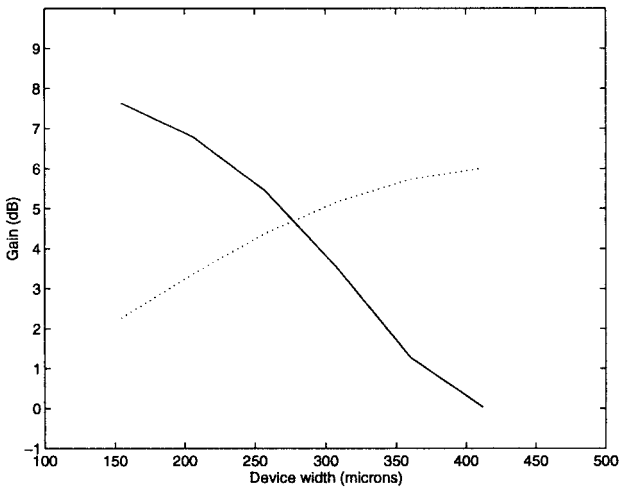

Fig. 13. RF gain of the MESFET as a function of device width. Frequency $= 10$ GHz (solid line) and 100 GHz (dotted line).

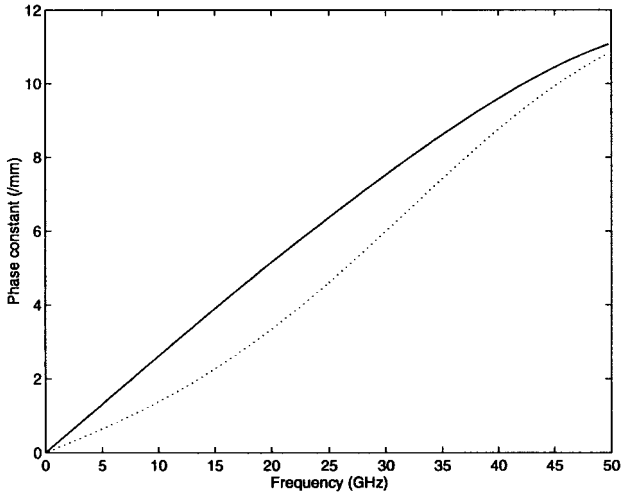

Fig. 14. Phase constant as a function of frequency. Gate mode (solid line). Drain model (dotted line).

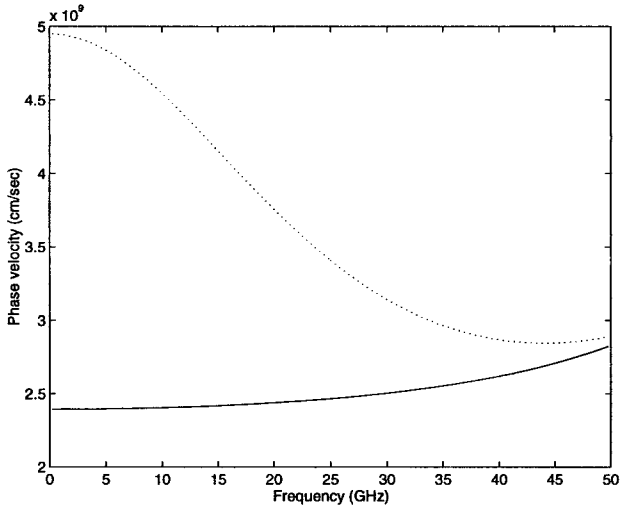

Fig. 15. Phase velocity as a function of frequency. Gate mode (solid line). Drain model (dotted line).

definition:

$$\text{Gain} = 20 \times \log_{10}\left(\frac{V_o(\omega, z)}{V_i(\omega, z_o)}\right) \tag{11}$$

where $V_i(\omega, z)$ and $V_o(\omega, z)$ are the Fourier transforms of the time-domain input and output signals, respectively. The input voltage is computed at a given reference plane some distance away from the excitation plane, while the output voltage is evaluated at different points along the device width.

The results for the gain as a function of frequency and device width are shown in Figs. 12 and 13, respectively. From these results, we can point out the following observations. At low frequencies, corresponding to operating wavelengths much larger than the device width, the gain increases steadily with increasing device widths. This observation is in accordance with well-established experimental and theoretical results about traveling-wave transistors. This is better indicated in Fig. 13, which shows that at a frequency of 10 GHz, corresponding to a wavelength of about 1 cm, increasing the device width from 100 to 450 μm leads to a monotonic increase in the gain. Note that, at this frequency, the maximum device width is well below 1/10 wavelength and, thus, negative distributed effects are still negligible. The steady increase in the gain is due to the increase in the overall transconductance of the device as its width is increased. As the frequency increases, the operating wavelength becomes on the order of the device width and traveling-wave effects on the device performance start to be clearly observed. We see that the device gain no longer increases as the device is made wider. This is clearly depicted by Fig. 13, which shows that at a frequency of 100 GHz, corresponding to a wavelength on the order of 100 μm, the gain monotonically decreases with increased device width. Since ohmic losses are neglected in this analysis, the gain reduction is due to traveling-wave effects, namely, phase cancellation between the input and output signals.

The phase mismatch between the input and output signals can be clearly observed from the propagation constant results. In Figs. 14 and 15, we show the frequency dependence of the phase constant and the phase velocity of the gate and

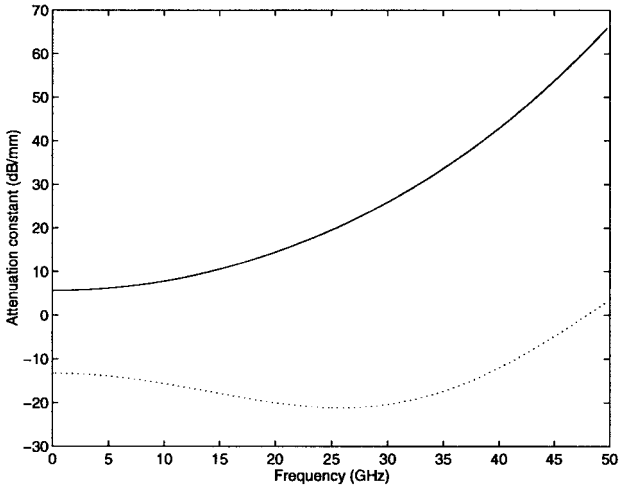

Fig. 16. Attenuation constant as a function of frequency. Gate mode (solid line). Drain model (dotted line).

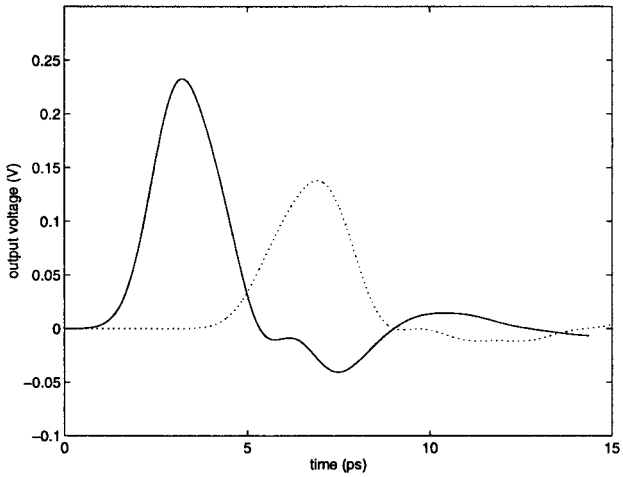

Fig. 17. Propagation delays of the output signal for the ABG MESFET (solid line) and for the conventional MESFET (dotted line).

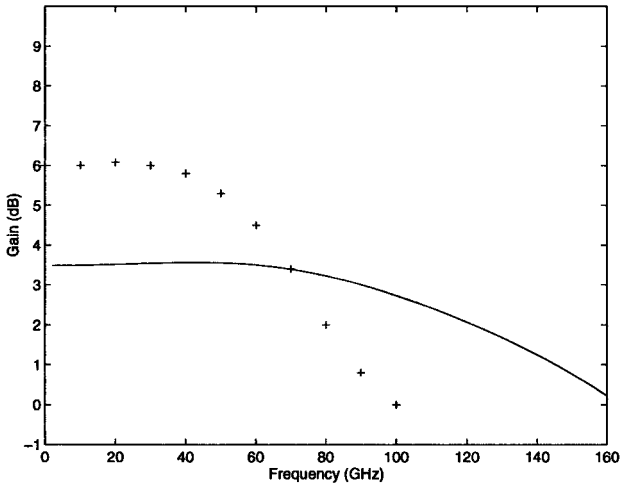

Fig. 18. Gain as a function of frequency for a 100 μm-wide device. ABG MESFET (solid line). Conventional MESFET (+++).

drain modes. These results clearly show that both modes propagate with different phase velocities. This difference is due to the different input impedance of the gate and drain electrodes, which is caused by the nonsymmetry of the field-effect transistor (FET) structure when operated in the common source mode and by the different bias voltages applied on the gate and drain. It is also interesting to note the strong dependence of the drain-mode phase velocity on frequency. On the other hand, the gate-mode phase velocity is much less sensitive to frequency. In other words, the gate and drain electrodes have noticeably different dispersive characteristics, with the drain electrode being much more dispersive than the gate electrode.

The results for the attenuation constant at the gate and drain electrodes are shown in Fig. 16. This figure shows that at lower frequencies, the drain mode has a negative attenuation constant corresponding to growing modes. Those growing modes are slowly suppressed as the operating frequency is increased. High attenuation constant for the gate model indicates that the input signal at the gate electrode is strongly attenuated. This attenuation increases monotonically with frequency. The fact that we neglected the electrodes metallic resistance indicates that this attenuation is due to substrate losses and losses in the active region. These losses are usually ignored in equivalent-circuit models.

This full-wave analysis clearly indicates that in addition to ohmic losses, the gain and bandwidth of microwave transistors are further degraded by phase cancellation between the input and output signals. This effect is more pertinent to high-frequency applications where more complex RF behavior of the device starts to take place. This behavior can be fully accounted for only through the inclusion of EM-wave propagation effects in the device model. In the light of the new full-wave results obtained, the high-frequency advantages of ABG devices over conventional devices become more obvious. The combination of high power handling capability and the relatively frequency-independent characteristics of ABG devices make them very attractive and potentially good competitors to conventional devices in various applications.

C. Full-Wave Simulation of the ABG MESFET

To show the RF characteristics of the ABG MESFET, a full-wave simulation was performed. In this simulation, the device was excited uniformly along its width. The input signal is applied between the source and gate electrodes. The output signal is collected between the drain and source at different points along the device width. The height of the ABG is taken to be 1 μm. The remaining simulation parameters are taken the same as for the planar MESFET.

For the ABG MESFET, the signal propagates along the device length, which is normally very short and, therefore, the signal propagation time is expected to be shorter than for planar MESFET's. This results is depicted clearly in Fig. 17. In this figure, we see that, for the ABG MESFET, the propagation time for the output signal is approximately 2.5 ps, whereas, for the planar MESFET, this time is about 7.5 ps (almost three times that of the ABG MESFET). This property of the ABG MESFET is expected to provide faster devices with better gain characteristics at high frequencies.

In Fig. 18, the gains of both the ABG MESFET and conventional MESFET are given as functions of frequency. From this

figure, we observe that, at lower frequencies, the conventional MESFET has higher gain values. On the other hand, the ABG MESFET has higher cutoff frequencies and provides constant gain values over wider frequency ranges than the conventional MESFET. These results can be explained by the fact that the ABG MESFET has a larger input capacitance $C_{\rm gs}$, which has the effect of reducing the overall device gain. It is important to note, however, that the dramatic reduction in the gain of the ABG MESFET is actually exaggerated by the fact that we used very small height for the ABG. This is done in order to reduce the amount of computer memory requirement. In practice, the gate is on the order of several microns high and the values of $C_{\rm gs}$ are much lower, leading to higher gain values than what is predicted by this simulation. As the frequency is increased, degradation of the device gain becomes predominantly due to traveling-wave effects, such as phase cancellation between the input and output signals. As mentioned earlier in this paper, these effects are significantly reduced in the case of the ABG MESFET, leading to better performance of the device and higher gain values at higher frequencies. Finally, one should note that since the ABG device is primarily intended for higher frequency applications, the low gain of the device at lower frequencies is not very critical, compared to the advantages the device provides at higher frequencies.

IV. Conclusion

In this paper, the potential performance of the ABG transistor as a low loss wide-band device was investigated. The investigation was first done from the dc point-of-view using a quasi-static semiconductor model. The preliminary results obtained from this model suggested that this new device have higher parasitic capacitance, lower bandwidth, and less gain than the conventional device. Although these results might be correct for low-frequency application, they have been proven to be totally misleading at high frequencies. At very high frequencies, several interesting phenomena with strong impact on the device behavior start to take place. Particle-wave interaction and phase cancellation effects are examples of such phenomena. Accurate simulation of these high-frequency effects can only be done through a full-wave modeling approach.

The paper also described a full-wave physics-based model. This model combines both accurate modeling of transport phenomena in short-channel devices and traveling-wave effects present at high operating frequencies. The model was successfully used to analyze the RF performance of both conventional and ABG MESFET devices. The results generated showed that the air-bridged MESFET has wider bandwidth and higher gains at high operating frequencies than the conventional MESFET. From these results, one can justify the idea of seriously considering ABG devices as alternatives to conventional devices for high-power high-frequency applications.

References

[1] S. M. El-Ghazaly and T. Itoh, "Traveling-wave inverted-gate field-effect transistors: Concepts, analysis and potential," *IEEE Trans. Microwave Theory Tech.*, vol. 36, pp. 1027–1032, Jan. 1989.

[2] W. Heinrich and H. L. Hartnagel, "Wave propagation on MESFET electrodes and its influence on transistor gain," *IEEE Trans. Microwave Theory Tech.*, vol. MTT-35, pp. 1–8, Jan. 1987.

[3] P. G. K. H. Kretschmer and T. Sigula, "Coupled-mode analysis of traveling-wave transistors," *Int. J. Electron.*, vol. 58, pp. 639–648, 1985.

[4] R. L. Kuvas, "Equivalent circuit model of FET including distributed gate effects," *IEEE Trans. Electron Devices*, vol. ED-27, pp. 1193–1195, June 1980.

[5] M. A. Al-Sunaidi and S. M. El-Ghazaly, "Electron-wave interaction in submicrometer gate field-effect transistors," in *IEEE MTT-S Dig.*, Sept. 1995, pp. 1257–1260.

[6] M. A. Al-Sunaidi and S. M. S. Imtiaz, and S. M. El-Ghazaly, "Electromagnetic wave effects on microwave transistors using a full-wave time-domain model," *IEEE Trans. Microwave Theory Tech.*, vol. 44, pp. 799–808, June 1996.

[7] S. M. S. Imtiaz and S. M. El-Ghazaly, "Global modeling of millimeter-wave circuits: Electromagnetic simulation of amplifiers," *IEEE Trans. Microwave Theory Tech.*, vol. 45, pp. 2208–2216, Dec. 1997.

[8] S. M. El-Ghazaly and T. Itoh, "Inverted-gate field-effect transistor: Novel high frequency structure," *IEEE Trans. Electron Devices*, vol. 1, pp. 19–30, Jan. 1988.

[9] Y. Chen, private communication.

[10] S. M. El-Ghazaly and T. Itoh, "Two-dimensional numerical simulation of short," *Int. J. Numer. Modeling*, vol. 1, pp. 19–30, Jan. 1988.

[11] S. M. El-Ghazaly, R. P. Joshi, and R. O. Grondin, "Electromagnetic and transport considerations in subpicosecond photoconductive switch modeling," *IEEE Trans. Microwave Theory Tech.*, vol. 38, p. 5, May 1990.

[12] B. Carnez, A. Cappy, A. Kaszynsky, E. Constant, and G. Salmer, "Modeling of a submicrometer gate field-effect transistor including effects of nonstationary electron dynamics," *J. Appl. Phys.*, vol. 51, pp. 784–790, Jan. 1980.

[13] R. Cook and J. Frey, "Two-dimensional numerical simulation of energy transport effects in Si and GaAs MESFET's," *IEEE Trans. Electron Devices*, vol. ED-29, pp. 970–977, June 1982.

[14] C. M. Snowden and D. Loret, "Two-dimensional hot-electron models for short-gate-length GaAs MESFET's," *IEEE Trans. Electron Devices*, vol. ED-34, pp. 212–223, Feb. 1987.

[15] Y. K. Feng and A. Hintz, "Simulation of submicrometer GaAs MESFET's using a full dynamic transport model," *IEEE Trans. Electron Devices*, vol. 35, pp. 1419–1431, Sept. 1988.

[16] K. Boltekjaer, "Transport equations for electrons in two-valley semiconductors," *IEEE Trans. Electron Devices*, vol. ED-12, pp. 38–47, Jan. 1970.

[17] A. S. Podgorski and L. Y. Wei, "Theory of traveling-wave transistors," *IEEE Trans. Electron Devices*, vol. ED-29, pp. 1845–1852, Dec. 1982.

[18] K. Frike and H. L. Hartnagel, "Experimental study of MESFET traveling-wave structures," *Int. J. Electron.*, vol. 58, pp. 629–638, 1985.

[19] Y. T. A. Higashisaka and F. Hasegawa, "High-power GaAs MESFET with an experimentally optimized pattern," *IEEE Trans. Electron Devices*, vol. ED-6, p. 1025, June 1980.

[20] S. E. Laux, "Techniques for small-signal analysis of semiconductor devices," *IEEE Trans. Electron. Devices*, vol. ED-32, pp. 2028–2037, Oct. 1985.

[21] K. E. Yee, "Numerical solution of initial boundary value problems involving Maxwell's equations in isotropic media," *IEEE Trans. Antennas Propagat.*, vol. AP-14, pp. 302–307, 1966.

[22] X. Z. Kenneth and K. Mei, "Time-domain finite difference approach to the calculation of the frequency-dependent characteristics of microstrip discontinuities," *IEEE Trans. Microwave Theory Tech.*, vol. 36, pp. 1775–1787, Dec. 1988.

[23] J. P. Berenger, "A perfectly matched layer for the absorption of electromagnetic waves," *J. Comput. Phys.*, vol. 114, pp. 185–200, 1994.

[24] ——, "Perfectly matched layer for the FDTD solution of wave-structure interaction problems," *IEEE Trans. Antennas Propagat.*, vol. 44, pp. 110–117, Jan. 1996.

[25] ——, "Three dimensional perfectly matched layer for the absorption of electromagnetic waves," *J. Comput. Phys.*, vol. 127, pp. 363–379, 1996.

[26] G. Mur, "Absorbing boundary conditions for the finite-difference approximation of the time-domain electromagnetic-fields equations," *IEEE Trans. Electromag. Compat.*, vol. EMC-23, pp. 377–382, Nov. 1981.

[27] D. N. Buechler, D. H. Roper, C. H. Durney, and D. A. Christensen, "Modeling sources in the FDTD formulation and their use in quantifying source and boundary condition errors," *IEEE Trans. Microwave Theory Tech.*, vol. 43, pp. 810–814, Apr. 1995.

[28] P. J. Roache, *Computational Fluid Dynamics*. Albuquerque, NM: Hermosa, 1972.

[29] K. S. Kunz, *Finite Difference Time Domain Method for Electromagnetics*. Boca Raton, FL: CRC Press, 1993.

[30] M. A. Al-Sunaidi, S. M. Hammadi, and S. M. El-Ghazaly, "Parallel implementation of a two-dimensional hydrodynamic model for microwave semiconductor device including inertia effects in momentum relaxation," *Int. J. Numer. Modeling*, vol. 10, pp. 107–119, 1997.
[31] A. Taflove, *Computational Electrodynamics, The Finite-Difference Time-Domain Method*. Norwood, MA: Artech House, 1995.
[32] G.-C. Liang, Y.-W. Liu, and K. K. Mei, "Full-wave analysis of coplanar waveguide and slotline using the time-domain finite-difference method," *IEEE Trans. Microwave Theory Tech.*, vol. 37, pp. 1949–1957, Dec. 1989.

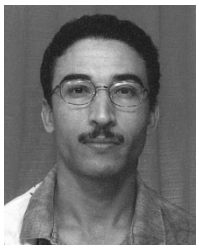

Samir M. Hammadi (S'96) was born in Kebili, Tunisia, in 1966. He received the B.S. degree in electrical engineering from Colorado State University, Fort Collins, in 1990, the M.S. degree in electrical engineering and electromagnetics, and the M.N.S. degree in applied and computational mathematics from Arizona State University, Tempe, in 1993 and 1994, respectively, and is currently working toward the Ph.D. degree in electrical engineering at the same university.

His research interest is in the numerical modeling of solid-state microwave devices and circuits.

Mr. Samir is a member of Tua Beta Pi and the American Mathematical Society.

Samir M. El-Ghazaly (S'84-M'86-SM'91), for photograph and biography, see this issue, p. 815.